Supercritical metalens at h-line for high-resolution direct laser writing

Jichao Fu[1†], Mengting Jiang[1†], Zeng Wang[1], Yi Fan Chen[1], Yuanda Liu[1], Qing Yang Steve Wu[1], Ai Jia Sim[1], Jiang Wang[1,2], Mingxi Chen[1], Ziyu Wang[1], Jie Deng[1], Xiao Song Eric Tang[1], Kun Huang[3], Hong Liu[1] and Jinghua Teng[1]*

Supercritical lens (SCL) can break the diffraction limit in the far field and has been demonstrated for high-resolution scanning confocal imaging. Its capability in sharper focusing and needle-like long focal depth should allow high-resolution lithography at violet or ultraviolet (UV) wavelength, however, this has never been experimentally demonstrated. As a proof of concept, in this paper SCLs operating at 405 nm (h-line) wavelength with smaller full-width-at-half-maximum focal spot and longer depth of focus than conventional Fresnel zone lens while maintaining controlled side lobes are designed for direct laser writing (DLW) lithography. Aluminum nitride (AlN) with a high refractive index and low loss in UV-visible range is used to fabricate nanopillar-based metasurfaces structure for the metalens. Grating arrays with improved pitch resolution are fabricated using the SCLs with sub-diffraction-limit focusing capability. The AlN-based metasurface for SCLs at short wavelength for DLW could extend further to UV or deep UV lithography and might be of great interest to both the research and industry applications.

Keywords: metalens; direct laser writing; supercritical lens; diffraction limit; ultraviolet metasurface

Introduction

Diffraction limit determines the ultimate resolution in a lithography system. Conventional lenses are constrained in the resolution, denoted by Abbe's diffraction limit: the full width at half maximum (FWHM) is approximately $0.5 \times \lambda/NA$[1], where λ is the wavelength and NA is the numerical aperture of the lens. To obtain smaller feature size and higher resolution, light sources of shorter wavelength λ are needed on one hand and lenses of higher NA and better performance on the other[2–5]. As wavelength approaches ultraviolet (UV), the fabrication of conventional bulky lenses becomes increasingly challenging, and available materials become fewer as most dielectrics start to absorb light strongly.

Metalenses are planar and ultrathin alternatives to conventional lenses[6–9]. They are made of resonant nanostructures with wavelength-scale thickness and have great versatility in functionalities[6–15] such as achromatic

[1]Institute of Materials Research and Engineering (IMRE), Agency for Science, Technology and Research (A*STAR), 2 Fusionopolis Way, Innovis #08-03, Singapore 138634, Singapore; [2]School of Microelectronics, Hefei University of Technology, Hefei 230009, China; [3]Department of Optics and Optical Engineering, University of Science and Technology of China, Hefei 230026, China.
†These authors contributed equally to this work.
*Correspondence: JH Teng, E-mail: jh-teng@imre.a-star.edu.sg

lenses[16–18], high-NA lenses[19], and polarization-switchable lenses[7]. Superoscillatory lenses (SOLs) have attracted much attention as they can break the diffraction limit in the far field and have an extended depth of focus, in which cases the optical fields oscillate locally faster than its highest Fourier spectrum components[20–22]. The FWHM of the central focal peak can be of deep sub-wavelength, however, the intensity of the central peak will decrease and that of the side lobes will increase exponentially, restraining the favorable application scenarios of SOLs. A good balance between the FWHM of the central focal spot and the side lobes is reached in the supercritical lenses (SCLs)[23,24] which have a focusing spot between $0.50\lambda/NA$ and $0.38\lambda/NA$ and a side lobe below 16.2% of the central peak. SOLs and SCLs have been demonstrated in focusing[25–28] and imaging applications[29–32]. SCLs are also proposed for lithography and data-storage applications[33] to pattern smaller features and mitigate the requirements on positioning by taking advantage of their higher resolution and longer depth of focus. However, to the best of our knowledge, there has been no such experimental demonstration yet in lithography, an important application to the semiconductor industry, photonics, and nanotechnology development. Different from imaging where the central focal spot plays the key role in determining the resolution, the side lobes from the SCLs have direct impacts on the lithography process and should be managed with special care, making the design of SCLs more challenging.

For a high-efficiency metalens, it is usually expected to have the meta antenna covering a phase range of 2π or more, which could be demanding on the materials and fabrications at short wavelengths[34]. Alternatively, binary modulated metalenses, like the Fresnel zone lenses (FZLs) which dramatically ease the challenges on metalens fabrication, have been proven to be a viable solution at short wavelengths[35]. Appropriate materials should be chosen to construct such metalenses working at violet or UV wavelength for lithography[36]. Silicon (Si) and titanium dioxide (TiO_2) are commonly used for metalenses working at near infrared and visible wavelengths, respectively, but they have strong absorbance at the wavelengths near and below 400 nm. Recently, dielectrics like niobium pentoxide (Nb_2O_5)[37], hafnium oxide (HfO_2)[38], and aluminium nitride (AlN)[39], two-dimensional materials[25], and void/air[34,40] have been proposed as alternative materials for UV nanophotonics. Among them, AlN is a promising candidate as it has a large band gap and matured fabrication process in industry.

Here, we report for the first time the binary modulated SCLs made of AlN-based metasurface that can focus 405 nm light beyond the diffraction limit in the far field and show better performances than FZLs in direct laser writing (DLW) lithography. The electromagnetic fields in the far field of these metalenses are calculated using a vectorial diffraction formula, and two different SCLs with controlled sidelobes and ultrasmall FWHMs are optimized numerically and then fabricated using AlN. This work provides new insights to the design of UV metasurfaces and SCLs for lithography application.

Materials and methods

Numerical simulation and optimization

The SCLs are constructed using binary-phase-based nano-antennas made of AlN nanopillars. The transmission coefficients of AlN nanopillars are calculated by commercial software, Lumerical FDTD. Periodic boundary conditions are applied at the transverse directions ($\pm x$ and $\pm y$), and the top and bottom ($\pm z$) regions are bounded with perfectly matched layers. The AlN and the sapphire substrate are assigned with refraction indices of 2.11 and 1.70 at the working wavelength of 405 nm[41,42], respectively.

A vectorial diffraction formula[43] is derived (See Supplementary information) and then implemented in a Python program to calculate the electromagnetic fields in the far field. Particle swarm algorithm (python module "PySwarms") is used to optimize the AlN nanopillar arrangement in the SCLs. The cost function used is:

$$g = 10^4 \times \left(\frac{I[1]}{I[0]} \right)^{1.1} + 10^7 \times (I[0] < I_{\text{threshold}})$$
$$+ 10^6 \times \sum_{i=2}^{N} (I[i] > (c[i] \times I[0])) \ ,$$

where $I[0], I[1], I[i]$ are the intensities of the electric fields at $x = 0, 0.25, 0.68, 0.79,…, 5$ μm, y all at 0, respectively, $I_{\text{threshold}}$ and $c[i]$ are predefined constants. Smallest cost values are reached by such intensity distributions that have the smallest FWHM, an efficiency above the threshold and all sidelobes below the corresponding thresholds. One thousand iterations are run in a round of optimization with 40 particles in each iteration, and its time cost is several hours in a personal computer.

SCL fabrication and direct laser writing

Commercially available AlN on sapphire wafers (PAM-XIAMEN, China) are used for the SCL fabrication. The thickness of AlN is 200 nm and the refractive index of AlN is from the database[41]. Hydrogen silsesquioxane (HSQ) (spin for 90 s at 3000 rpm) is used as the e-beam lithography resist and also the mask layer for the dry-etching process. A chlorine-based recipe using inductively coupled plasma (ICP) etching at RF power of 130 W, bias voltage of 190 V, ICP power of 500 W, $BCl_3/Cl_2/He$ flow rate of 10/30/5 sccm[44,45] is optimized for AlN nanopillar etching. The remaining HSQ mask is removed by buffered HF solvent after the dry etching.

The DLW lithography is built upon a photon scanning tunneling microscope (PSTM) system (WITec, alpha300S). Figure 1(a) shows the principle of the DLW system using the AlN SCL. A light beam is emitted from a 405 nm continuous-wave laser (Cobolt 08-01 series, 30 mW), and a circular pinhole (PH) of 200 μm clear aperture is used as a spatial filter to improve the beam quality, followed by an attenuator (AT) to tune the light intensity. A pair of mirrors (M1 and M2) are used for tuning the beam direction, and the third mirror M3 is a 45-

degree corner reflecting mirror to change the beam direction from horizontal to vertical. A linear polarizer (LP) and a conventional lens (CL) with a focal length of $f = 200$ mm are inserted between M2 and M3. The conventional lens shrinks the laser beam size to match it with the size of metalenses to improve the total efficiency. Sample coated with photoresist is fixed on a piezo-stage and positioned at the focus plane of metalenses. The piezo and the motor stages in the PSTM system are used to move the samples during DLW. An objective lens (Olympus LMPlanApo, 250×/0.90) and a back-illuminated scientific Complementary Metal–Oxide–Semiconductor (sCMOS) camera (Andor Marana 4.2B-11) are used for measuring the focal patterns. A commercial h-line negative resist (Micro Resist maN-1405) is used for the DLW lithography. It is coated on quartz substrate at a spin speed of 3000 rpm for 60 s and then prebaked at 100 °C for 60 s resulting in a thickness of 500 nm. After DLW, the photoresist is developed in developer ma-D 533/S for around 20 s.

After spatial filtering (by PH), attenuating (by AT), polarizing (by LP), directing (by M1, M2 and M3) and size-adjusting (by CL), the 405 nm light beam upon ML
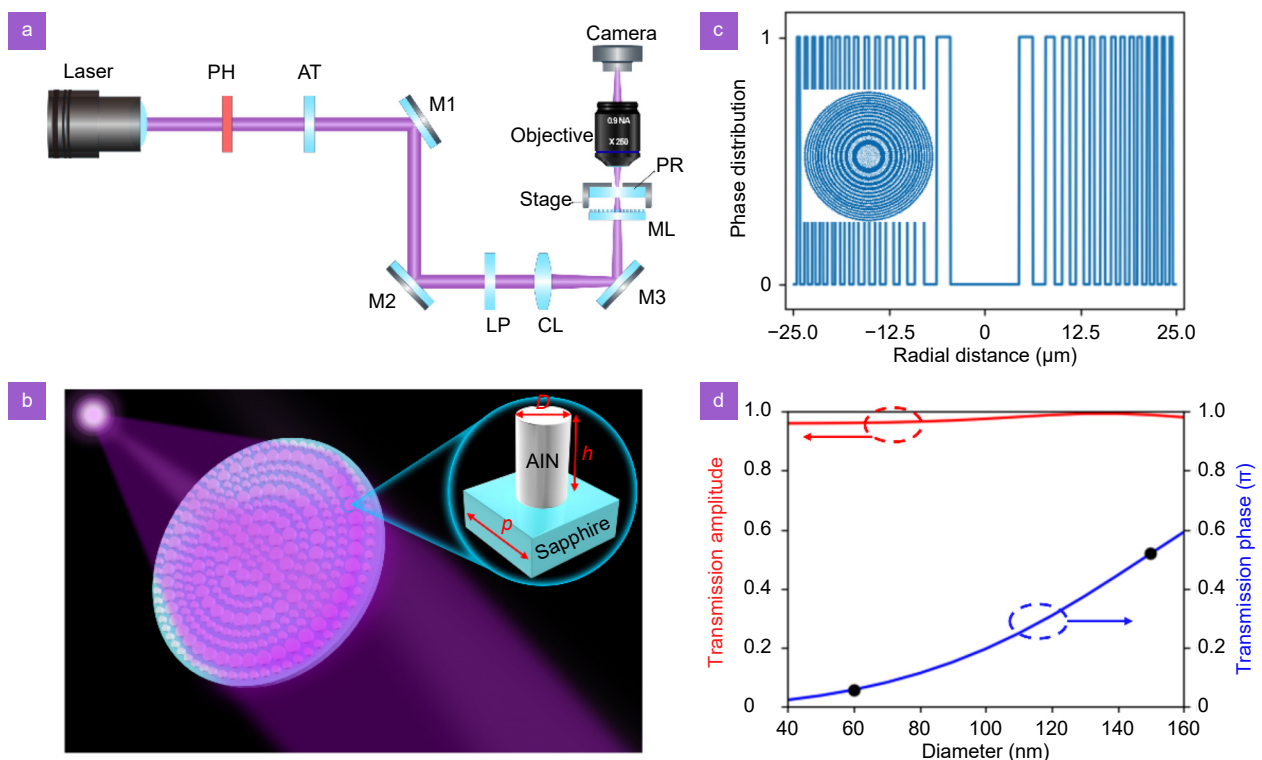
Fig. 1 | Metalens-based DLW lithography. Schematic diagrams of (**a**) the DLW lithography setup, (**b**) the metalens and its constructing unit cells. (**c**) The metalens in top view and cross-section view. (**d**) The amplitude and phase profile in transmission mode of the AlN unit cell with varying pillar diameters. PH, pinhole; AT, attenuator; M1, M2, M3, mirrors; LP, linear polarizer; CL, conventional lens; ML, metalens; PR, photoresist.

is a slightly converging high-purity Gaussian beam with a similar size to ML. The ML further focuses the beam onto the PR plane and exposes the resist while the wafer is moving laterally in a programmable way during the exposure. The moving trajectory determines the pattern to write and the moving speed determines the exposure dose.

Results and discussions

The SCLs are designed as binary-phase modulated metalens, where only two sizes of AlN nanopillars are needed. This dramatically eases the requirements on materials and fabrications, while keeping the versatility of metalens design. The AlN material has a very large bandgap (~ 6.2 eV) and is transparent at UV and even deep UV (DUV) wavelengths. It has a relatively high refractive index in the violet and UV range and can be easily etched with Cl_2-based plasma, thus making it a suitable material for metalenses especially in UV-DUV range. The proposed metalenses have a diameter of 50 μm and a focal length of 50 μm (Fig. 1(c)), yielding an NA of 0.45. AlN nanopillars with a height of h = 200 nm

and a pitch of p = 200 nm are located on sapphire substrate (Fig. 1(b)). Normalized to the wavelength of 405 nm, the thickness value here is much smaller than in other literatures[37,38], thus simplifying the fabrication. Pillars with diameters of 60 nm and 150 nm are chosen as unit "0" and "1", respectively, to obtain a phase difference of around 0.5π (Fig. 1(d)). Although this insufficient phase modulation will lead to the slight decrement of optical efficiency (See Supplementary information)[46], it is enough to make an SCL for DLW lithography as shown shortly in Fig. 2.

Taking the conventional FZL (Fig. 1(c)) as a control case, two SCLs (Figs. 2(a, b)) with smaller FWHMs and controlled side lobes are designed. Different from the concentric ring structures utilized in most literatures for FZLs and SCLs, each ring in our design is constructed by discrete nanopillars (Fig. 2(d)). Compared to ring structures, discrete circular nanopillar structures are truly polarization-insensitive, while elliptical pillar structures can be adopted in cases where polarization manipulation is needed to make devices with richer capabilities. The metalens of 50 μm diameter is divided into 125 concentric
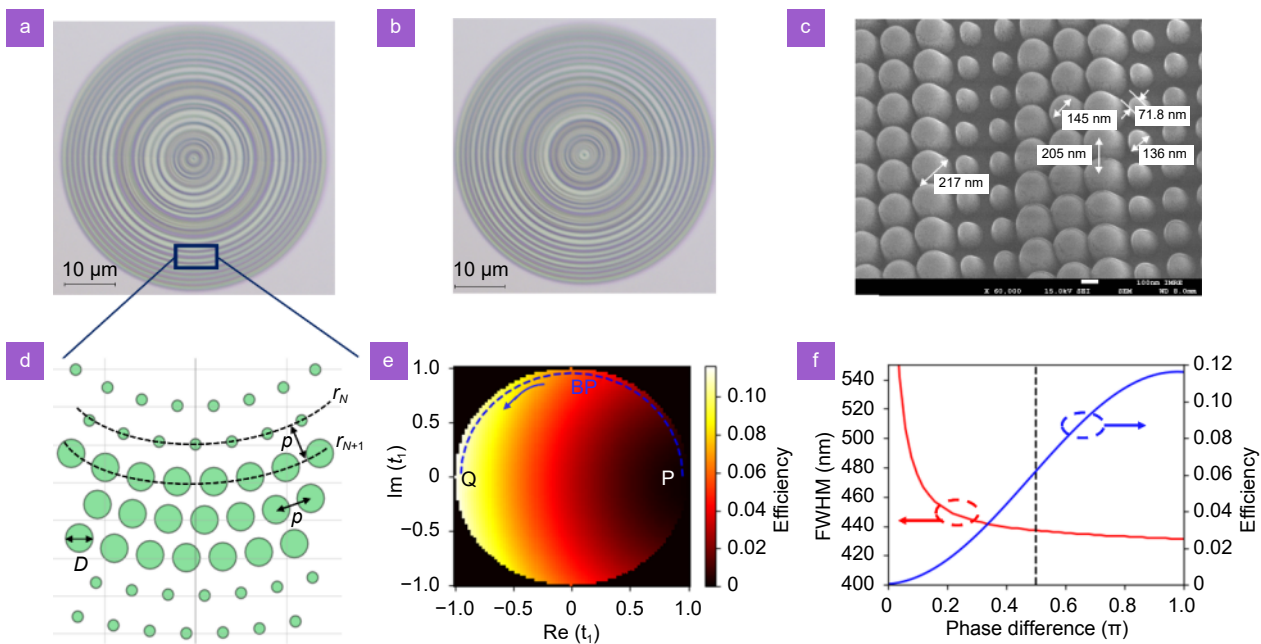
Fig. 2 | Design and fabrication of SCLs and FZL. Optical images of (**a**) SCL05 (the ratio of the intensities of the first side lobe and the central peak is 5%), (**b**) SCL10 (the ratio of the intensities of the first side lobe and the central peak is 10%). (**c**) Scanning electron microscopy (SEM) images of the FZL after all experiments and coated with a thin layer of gold. (**d**) Schematic diagram of an enlarged region in (a). (**e**) The efficiency of SCL05 with other possible selections of units "0" and "1". In this more general case, the unit "0" is assumed to have a transmission coefficient of t_0 = 1, and the unit "1" can have any physically reasonable transmission coefficient with transmission amplitude ≤1 and phase between 0 and 2π. The horizontal and vertical axes are the real and imaginary parts of the transmission coefficient of the permitted unit "1", respectively. (**f**) The changes of FWHM and efficiency of SCL05 when the unit "1" evolves from point P (t = 1) to point Q (t = −1) through the binary phase (BP) path in (e). The black dashed line indicates the unit "1" adopted in the final designs.

rings with an increment p = 200 nm in radial direction, resulting in a binary code of 125 digits. In each ring, unit "0" is filled by pillars with a diameter of 60 nm and unit "1" by pillars with a diameter of 150 nm. They are arranged with a distance of around p = 200 nm (a tiny deviation may arise from the discretization process). Full-wave simulation of metalenses with numerous and feature-small structures is highly costly in both resource and time. We simplify the design by firstly using full-wave simulation to get the responses of each unit (Fig. 1(d)) and then using a vectorial diffraction formula to handle the propagation part. The vectorial diffraction formula (see Supplementary information) with sufficient accuracy is much faster than full-wave simulation, meanwhile it can be easily integrated with optimization method like particle swarm algorithm.

The binary code of FZL can be obtained directly from the formula, $\varphi = \left(\sqrt{f^2 + r^2} - f \right) \times \frac{2\pi}{\lambda}$, where f is the designed focal length, r is the radial distance, and λ is the wavelength. For the Nth ring, if the residual of φ divided by 2π is between 0 and π, unit "0" is assigned, and if the residual is between π to 2π, unit "1" is assigned. Then the leftmost four digits of this 125-digit binary code, corresponding to the 0th ring to the 3rd ring, can be denoted by a one-digit hexadecimal number. Similar processes are applied to the 5th to 8th digits etc., and the FZL can be finally represented by a code of 000001FF00FC1F0F870E1C71CE318C0. The other two SCLs (i.e., SCL05 in Fig. 2(a) and SCL10 in Fig. 2(b)) with smaller FWHMs and controlled sidelobes are optimized to be 34B4CDAF9F7E670B650F3E71CE318C0 and 3DB4CDA51F76630B674F3E71CE398C0, respectively. Their simulated intensities of first side lobes are 0.05 and 0.10 of their central peaks, respectively. These three metalenses are fabricated using e-beam lithography and a Cl_2-based dry etching (see Materials and Methods). After the dry etching, pillars are completely engraved with a sidewall angle of over 80 degrees, as shown in the SEM images (Fig. 2(c)).

The performance in terms of FWHM and efficiency of SCL05 with other possible selections of units of "1" and "0" is characterized using the vectorial diffraction formula and presented in Fig. 2(e). In this more general case, the unit "0" is supposed to have a transmission coefficient of $t_0 = 1$, which can be met with no structure, and the unit "1" has a transmission amplitude no larger than 1 and a transmission phase between 0 and 2π. The location of unit "1" can thus be any point within (or on) the unit circle on the complex plane of the transmission coefficients showed in Fig. 2(e). When the unit "1" coincides with the unit "0" at point P, there is no focusing effect; when the unit "1" moves towards point Q ($t = -1$), the efficiency reaches its maximum. In the scenario of binary phase modulation where the unit "1" evolves from point P to point Q via the binary phase path (transmission amplitude is kept at 1 and transmission phase increases from 0 to π), the FWHM decreases gradually to 430 nm and the efficiency increases gradually to 11.7% (Fig. 2(f)), which are the attainable smallest FWHM and largest efficiency by using binary SCL05 under all possible selections of units "0" and "1". The final adopted units "0" and "1" in this paper (Fig. 1(d)) have transmission amplitudes of nearly 1 and a phase difference of 0.5π, resulting in a halved efficiency but a nearly equal FWHM compared to the full-π phase modulation scenario (Fig. 2(f)), which shows the tremendous advantage of binary modulation method in its robustness on FWHM. Similar results apply to the binary FZL, and we note that a binary phase modulation with a 0.5π phase difference is already better than a binary amplitude modulation with a full amplitude contrast (see Supplementary information).

The focusing patterns of these three metalenses are calculated by using the vectorial diffraction formula (Fig. 3(a–c)) and measured with a back-illuminated sCMOS camera in experiment (Fig. 3(d–f)). The focusing patterns in experiment, with a lower imaging resolution due to the finite pixel size (11 μm) of sCMOS camera, correspond quite well with the simulated results. For the FZL, the focal length, defined as the longitudinal position z of the peak intensity is calculated to be 50.28 μm (Fig. 3(a)) and measured to be 47.4 μm (Fig. 3(d)). For SCL05, the calculated and measured focal lengths are 49.83 μm (Fig. 3(b)) and 46.6 μm (Fig. 3(e)), respectively, while the SCL10 has calculated and measured focal lengths of 50.05 μm (Fig. 3(c)) and 47.2 μm (Fig. 3(f)), respectively. The measured focal lengths are all slighter closer by around 3 μm from the calculated ones, which is mainly caused by the non-collimated incident light. Importantly, the measured FWHMs of these three metalenses coincide perfectly with the simulated results, as confirmed in Fig. 3(g–i). The SCL05 and SCL10 exhibit smaller FWHMs below the diffraction limit, longer depths of focus than the FZL, meanwhile their side lobes are also well suppressed. Note that the FWHM of the focal spot in the
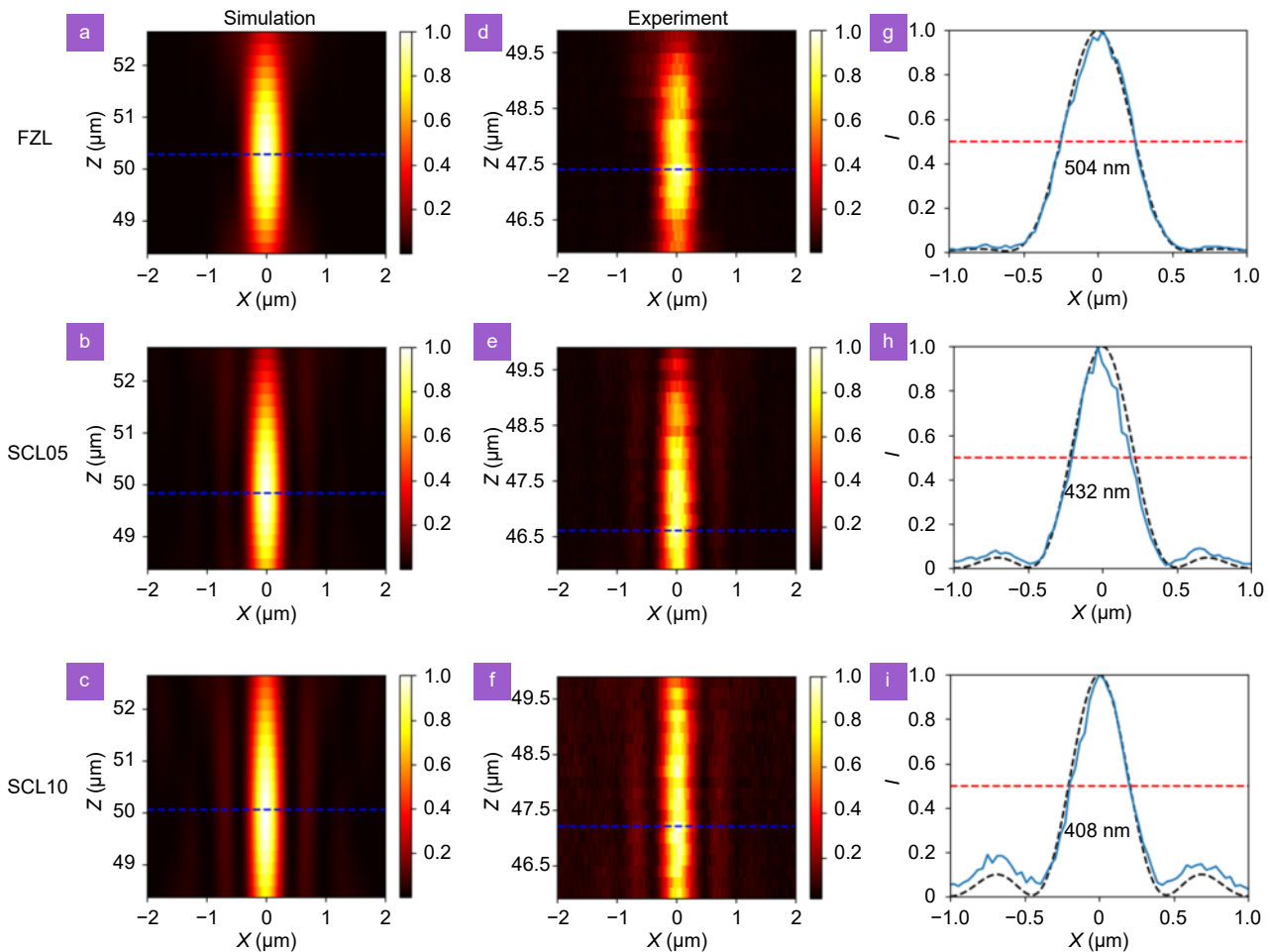
Fig. 3 | Focusing characteristics of the FZL and SCLs. (**a–c**) Intensities at *x-z* plane calculated by the vectorial diffraction formula. (**d–f**) Intensities measured. (**g–i**) Normalized intensities along *x* crossing the maximums (dashed black lines for analytic and solid blue lines for measured results) of which positions indicated by the blue dashed lines in (a-f). The calculated values of FWHMs are explicitly labelled. (a, d, g) correspond to FZL, (b, e, h) correspond to SCL05 and (c, f, i) correspond to SCL10.

FZL is larger than Abbe's criterion ($0.5 \times 405/NA = 452.8$ nm). One reason is that the incident wave is not a plane wave, but a Gaussian beam with a waist radius of 25 μm matching the size of the metalenses. Increasing the incident beam size can decrease the FWHM of the focal spot (see Supplementary information), but at a price of decreased efficiency and unwanted exposure at outer resist regions. SCL10 also shows a noticeable longer depth of focus than FZP, and especially its FWHM keeps nearly constant in the range of *z* from 46 to 54 μm (see Supplementary information). This extended depth of focus would alleviate the alignment requirement on *z* direction and benefit a lot in exposing thicker resist film.

These three metalenses are used to perform DLW in experiments. Five groups of gratings are written on commercial photoresists ma-N 1405. Each group consists of six 4 μm-long lines with their full pitches of 680, 650, 620, 590 and 560 nm, from the left to the right panels

(Fig. 4(a–c)). As the pitch decreases and approaches each focal spot size, the gap between two adjacent lines within the same group becomes shallower and more difficult to be resolved, which is similar to the imaging case. It can be calculated from the simulated FWHM (Fig. 3(g)) that the doses at the gap position are 53.5%, 61.2%, 69.2%, 75.4%, 83.5% of the doses at the line position, from the left to the right panels in Fig. 4(a), 28.5%, 35.5%, 43.4%, 49.9%, 59.4% in Fig. 4(b), and 19.1%, 25.2%, 32.3%, 38.4%, 47.5% in Fig. 4(c). The atomic force microscopy (AFM) images (Fig. 4(d–f)) also reveal that the SCLs have a stronger capability in writing high-resolution patterns than the FZL, as the contrast of all the grating patterns generated by the SCLs are better than those by the FZL. Taking the fifth group as an example, the patterns generated by the SCLs can be clearly resolved but those by the FZL are nearly unresolved. By adopting the similar methodology of identifying the resolution of
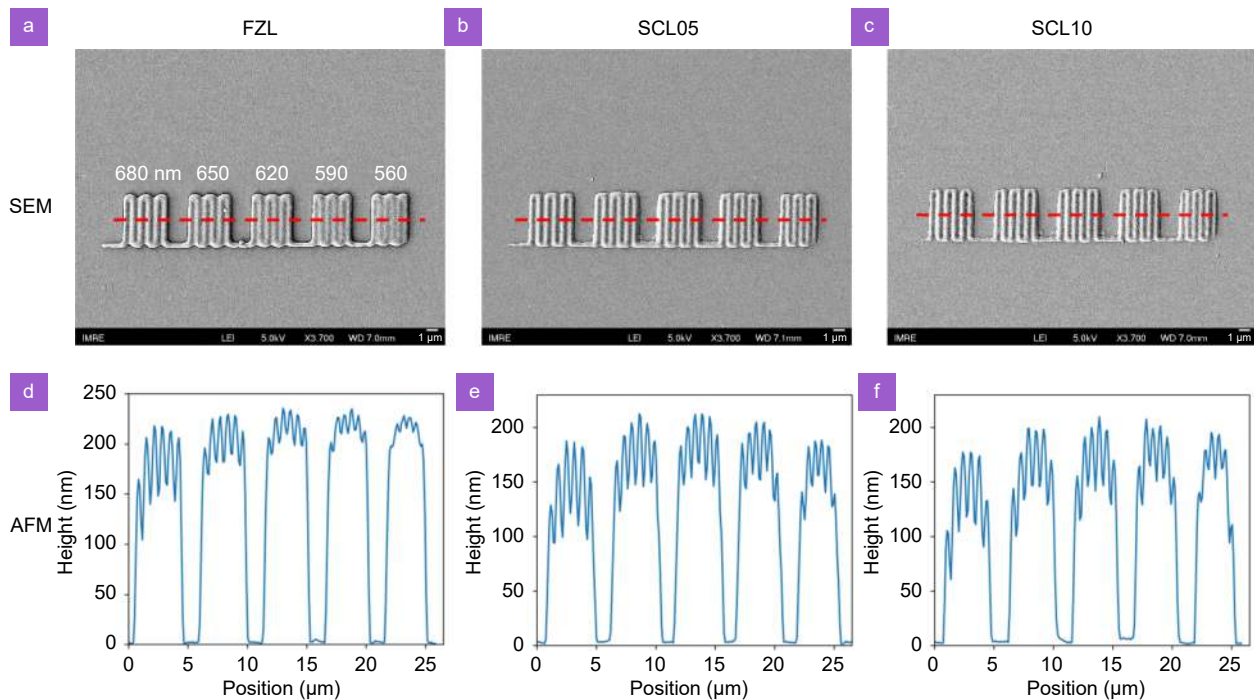
Fig. 4 | Grating patterns generated by the FZL- and SCL-based DLW. (**a–c**) SEM images of the grating patterns, from left to right, with pitches of 680, 650, 620, 590 and 560 nm and a length of 4 μm written by the FZL (a), SCL05 (b) and SCL10 (c). (**d–f**) Measured height information by AFM (atomic force microscopy) along the positions indicated by the red dashed lines in (a–c).

metalenses in imaging, resolutions of these metalenses can be found by writing lines with decreasing pitches until no pattern can be distinguished within one group. The resolutions of the FZL, SCL05 and SCL10 are found to be around 540, 500 and 480 nm, respectively (see Supplementary information). The SCLs show a nearly 10% improvement in resolution compared to the FZL. Note that, such an advantage of SCLs in lithography cannot be achieved for SOLs with unoptimized side lobes.

DLW method is an important complement to the projection-type lithography utilized widely in micro-fabrication and semiconductor industry. As a mask-free method, DLW provides a convenient, fast, efficient, and cost-effective solution to the fabrication of small- or medium-scale patterns with microfeatures, and thus are widely adopted in research and industry to fabricate micro-electro-mechanical system, photomask, and prototype patterns[47]. DLW can typically achieve a resolution of hundreds of nanometres, while further improvement in resolution is highly demanded to make it a strong competitor to the much more expensive and cumbersome e-beam lithography. The SCL method demonstrated here provides a new avenue to improve the resolution of DLW. With higher NA, shorter wavelength, and more judicious design, SCL-based DLW has the potential to push resolution to sub-100 nm or even sub-50 nm, to be

a more powerful technology for micro-nano-fabrication.

Conclusions

In summary, SCLs with capabilities of sub-diffraction-limit focusing have been demonstrated experimentally for high-resolution direct laser writing for the first time. AlN nanopillars are used to build the SCLs operating at 405 nm wavelength. The SCLs with delicately controlled sidelobes achieve better resolutions than the FZLs that are widely adopted at UV wavelengths. Two types of units yielding a phase difference of 0.5π are used to construct these binary-phase modulated SCLs with ultrasmall thickness, which releases the requirements on materials and fabrications. Our work suggests new approach to the design of SCLs and allows for wider applications of metalenses in lithography, laser-assisted micro- and nano-printing processing, and others.

References

1. Fischer J, Wegener M. Three-dimensional optical laser lithography beyond the diffraction limit. *Laser Photonics Rev* **7**, 22–44 (2013).
2. Smith HI. A review of submicron lithography. *Superlattices Microstruct* **2**, 129–142 (1986).
3. Ito T, Okazaki S. Pushing the limits of lithography. *Nature* **406**, 1027–1031 (2000).
4. Kneer B, Migura S, Kaiser W et al. EUV lithography optics for

sub-9nm resolution. *Proc SPIE* **9422**, 94221G (2015).

5. Zahlten C, Gräupner P, van Schoot J et al. High-NA EUV lithography: pushing the limits. *Proc SPIE* **11177**, 111770B (2019).

6. Yu NF, Genevet P, Kats MA et al. Light propagation with phase discontinuities: generalized laws of reflection and refraction. *Science* **334**, 333–337 (2011).

7. Arbabi A, Horie Y, Bagheri M et al. Dielectric metasurfaces for complete control of phase and polarization with subwavelength spatial resolution and high transmission. *Nat Nanotechnol* **10**, 937–943 (2015).

8. Huang K, Qin F, Liu H et al. Planar diffractive lenses: fundamentals, functionalities, and applications. *Adv Mater* **30**, 1704556 (2018).

9. Ha YL, Luo Y, Pu MB et al. Physics-data-driven intelligent optimization for large-aperture metalenses. *Opto-Electron Adv* **6**, 230133 (2023).

10. Arbabi A, Arbabi E, Horie Y et al. Planar metasurface retroreflector. *Nat Photonics* **11**, 415–420 (2017).

11. Lalanne P, Chavel P. Metalenses at visible wavelengths: past, present, perspectives. *Laser Photonics Rev* **11**, 1600295 (2017).

12. Ding F, Pors A, Bozhevolnyi SI. Gradient metasurfaces: a review of fundamentals and applications. *Rep Prog Phys* **81**, 026401 (2018).

13. Pan MY, Fu YF, Zheng MJ et al. Dielectric metalens for miniaturized imaging systems: progress and challenges. *Light Sci Appl* **11**, 195 (2022).

14. Gao H, Fan XH, Wang YX et al. Multi-foci metalens for spectra and polarization ellipticity recognition and reconstruction. *Opto-Electron Sci* **2**, 220026 (2023).

15. Li JT, Wang GC, Yue Z et al. Dynamic phase assembled terahertz metalens for reversible conversion between linear polarization and arbitrary circular polarization. *Opto-Electron Adv* **5**, 210062 (2022).

16. Ndao A, Hsu L, Ha J et al. l. Octave bandwidth photonic fishnet-achromatic-metalens. *Nat Commun* **11**, 3205 (2020).

17. Fan YB, Yao J, Tsai DP. Advance of large-area achromatic flat lenses. *Light Sci Appl* **12**, 51 (2023).

18. Wang YJ, Chen QM, Yang WH et al. High-efficiency broadband achromatic metalens for near-IR biological imaging window. *Nat Commun* **12**, 5560 (2021).

19. Paniagua-Domínguez R, Yu YF, Khaidarov E et al. A metalens with a near-unity numerical aperture. *Nano Lett* **18**, 2124–2132 (2018).

20. Huang K, Ye HP, Teng JH et al. Optimization-free superoscillatory lens using phase and amplitude masks. *Laser Photonics Rev* **8**, 152–157 (2014).

21. Chen G, Wen ZQ, Qiu CW. Superoscillation: from physics to optical applications. *Light Sci Appl* **8**, 56 (2019).

22. Zheludev NI, Yuan GH. Optical superoscillation technologies beyond the diffraction limit. *Nat Rev Phys* **4**, 16–32 (2022).

23. Qin F, Huang K, Wu JF et al. A supercritical lens optical label-free microscopy: sub-diffraction resolution and ultra-long working distance. *Adv Mater* **29**, 1602721 (2017).

24. Qin F, Liu BQ, Zhu LW et al. π-phase modulated monolayer supercritical lens. *Nat Commun* **12**, 32 (2021).

25. Wang Z, Yuan GH, Yang M et al. Exciton-enabled meta-optics in two-dimensional transition metal dichalcogenides. *Nano Lett* **20**, 7964–7972 (2020).

26. Dai XM, Dong FL, Zhang K et al. Holographic super-resolution metalens for achromatic sub-wavelength focusing. *ACS Photonics* **8**, 2294–2303 (2021).

27. Lu XJ, Guo YH, Pu MB et al. Broadband achromatic metasurfaces for sub-diffraction focusing in the visible. *Opt Express* **29**, 5947–5958 (2021).

28. Tang DL, Wang CT, Zhao ZY et al. Ultrabroadband superoscillatory lens composed by plasmonic metasurfaces for subdiffraction light focusing. *Laser Photonics Rev* **9**, 713–719 (2015).

29. Rogers ETF, Lindberg J, Roy T et al. A super-oscillatory lens optical microscope for subwavelength imaging. *Nat Mater* **11**, 432–435 (2012).

30. Gbur G. Using superoscillations for superresolved imaging and subwavelength focusing. *Nanophotonics* **8**, 205–225 (2019).

31. Li Z, Zhang T, Wang Y et al. Achromatic broadband super‐resolution imaging by super‐oscillatory metasurface. *Laser Photonics Rev* **12**, 1800064 (2018).

32. Zhang RZ, Guo YH, Li XY et al. Angular superoscillatory metalens empowers single‐shot measurement of OAM Modes with finer intervals. *Adv Opt Mater* **12**, 2300009 (2024).

33. Yuan GH, Rogers ETF, Roy T et al. Planar super-oscillatory lens for sub-diffraction optical needles at violet wavelengths. *Sci Rep* **4**, 6333 (2014).

34. Ossiander M, Meretska ML, Hampel HK et al. Extreme ultraviolet metalens by vacuum guiding. *Science* **380**, 59–63 (2023).

35. Salmassi F, Naulleau PP, Gullikson EM et al. Extreme ultraviolet binary phase gratings: fabrication and application to diffractive optics. *J Vac Sci Technol A* **24**, 1136–1140 (2006).

36. Zhao D, Lin ZL, Zhu WQ et al. Recent advances in ultraviolet nanophotonics: from plasmonics and metamaterials to metasurfaces. *Nanophotonics* **10**, 2283–2308 (2021).

37. Huang K, Deng J, Leong HS et al. Ultraviolet metasurfaces of ≈80% efficiency with antiferromagnetic resonances for optical vectorial anti‐counterfeiting. *Laser Photonics Rev* **13**, 1800289 (2019).

38. Zhang C, Divitt S, Fan QB et al. Low-loss metasurface optics down to the deep ultraviolet region. *Light Sci Appl* **9**, 55 (2020).

39. Hu ZL, Long LY, Wan RQ et al. Ultrawide bandgap AlN metasurfaces for ultraviolet focusing and routing. *Opt Lett* **45**, 3466–3469 (2020).

40. Hentschel M, Koshelev K, Sterl F et al. Dielectric Mie voids: confining light in air. *Light Sci Appl* **12**, 3 (2023).

41. Beliaev LY, Shkondin E, Lavrinenko AV et al. Thickness-dependent optical properties of aluminum nitride films for mid-infrared wavelengths. *J Vac Sci Technol A* **39**, 043408 (2021).

42. Boidin R, Halenkovič T, Nazabal V et al. Pulsed laser deposited alumina thin films. *Ceram Int* **42**, 1177–1182 (2016).

43. Kim J, Wang Y, Zhang X. Calculation of vectorial diffraction in optical systems. *J Opt Soc Am A* **35**, 526–535 (2018).

44. Liu XW, Sun CZ, Xiong B et al. Smooth etching of epitaxially grown AlN film by Cl2/BCl3/Ar-based inductively coupled plasma. *Vacuum* **116**, 158–162 (2015).

45. Pinto RMR, Gund V, Calaza C et al. Piezoelectric aluminum nitride thin-films: a review of wet and dry etching techniques. *Microelectron Eng* **257**, 111753 (2022).

46. He J, Zhao D, Liu H et al. An entropy-controlled objective chip for reflective confocal microscopy with subdiffraction-limit resolution. *Nat Commun* **14**, 5838 (2023).

47. Wang S, Zhou Z, Li B et al. Progresses on new generation laser direct writing technique. *Mater Today Nano* **16**, 100142 (2021).

This is an early view version and will be formally published in a coming issue with other articles in due time.

Author contributions

JC Fu and MT Jiang contributed equally to this work. JC Fu, JH Teng conceived the ideas. JC Fu performed the design. MT Jiang, JC Fu and Z Wang built the DLW setup. JC Fu, MT Jiang, YF Chen, QYS Wu, J Deng, and XSE Tang fabricated the samples. JC Fu performed the DLW experiments. JC Fu, MT Jiang, YD Liu, AJ Sim, J Wang, MX Chen, ZY Wang performed the metalens measurements and characterizations. K Huang and H Liu contributed to the SCLs design and laser writing. JH Teng supervised the project. JC Fu and JH Teng wrote the manuscript. All the authors discussed the results, analyzed the data, and commented on the manuscript.

Competing interests

The authors declare no competing financial interests.

Supplementary information

Supplementary information for this paper is available at
https://doi.org/10.29026/oes.2024.230035